In vitro dissolution and characterization of flame-sprayed bioactive glass microspheres S53P4 and 13-93

Sinitsyna, Polina; Karlström, Oskar; Sevonius, Christoffer; Hupa, Leena

Published in:
Journal of Non-Crystalline Solids

DOI:
https://doi.org/10.1016/j.jnoncrysol.2022.121736
10.1016/j.jnoncrysol.2022.121736

Published: 01/01/2022

Document Version
Final published version

Document License
CC BY

Journal of Non-Crystalline Solids 591 (2022) 121736

Contents lists available at ScienceDirect

Journal of Non-Crystalline Solids

journal homepage: www.elsevier.com/locate/jnoncrysol

In vitro dissolution and characterisation of flame-sprayed bioactive glass microspheres S53P4 and 13–93

Polina Sinitsyna [a,*], Oskar Karlström [a], Christoffer Sevonius [a,b], Leena Hupa [a,*]

[a] Johan Gadolin Process Chemistry Centre, Åbo Akademi University, Henrikinkatu 2, Turku 20500, Finland
[b] Bonalive Biomaterials Ltd., Biolinja 12, Turku 20750, Finland

ARTICLE INFO

Keywords:
Bioactive glass microspheres
S53P4, Flame-spraying
Dynamic dissolution
Ion release
In vitro bioactivity

ABSTRACT

Microspheres based on the bioactive glass S53P4 were successfully produced through flame-spraying. Glass 13–93 microspheres were utilised as a reference composition with a known behaviour in flame spheroidisation. Bioactive glass microspheres (BGMs) enable a range of advantages compared to conventional irregular-shaped particles. The produced BGMs in size ranges of 45–90 and 90–125 μm were characterised by DTA, SEM/EDXA, FTIR, and XRD. Dynamic dissolution experiments were carried out using TRIS buffer and SBF (pH 7.4) for 72 h. The ion concentrations in the solutions were measured using ICP-OES. The *in vitro* bioactivity results indicated that the hydroxyapatite (HA) layer was thicker for the larger spheres after dissolution in SBF. According to the SEM-EDXA results, the S53P4 spheres showed a more rapid formation of the hydroxyapatite layer than the reference 13–93. The thermal and *in vitro* properties of the BGMs were similar to the particles of the parent glasses. The results suggest that microspheres based on S53P4 bioactive glass have an excellent potential for future clinical applications.

1. Introduction

Since their discovery in the 1960s, bioactive glasses have found several applications in biomedicine [1]. In the body fluids, silicate-based bioactive glasses in the Na_2O–CaO–P_2O_5–SiO_2 system form a calcium phosphate surface layer that chemically bonds the glass to living tissue [2]. Cell culture, *in vitro,* and clinical studies also confirm the ability of bioactive glasses to stimulate and guide the regeneration of bone and soft tissues [3,4-8]. To provide the desired biological interaction, described as controlled ion release followed by tissue bonding, the silica content of the glass must be between 45 and 55 wt.% [9]. The lower the silica content, the easier the glass dissolves in different aqueous solutions. However, glasses with more than 60 wt.% of SiO_2 dissolve so slowly that they do not form silica-rich and calcium phosphate (CaP) reaction layers at the glass surface [10,11]. Consequently, such glasses are not likely to bond to bone and soft tissues. Spherical-shaped particles have been assumed to provide beneficial properties for biomedical applications compared to irregular particles. For example, bioactive glass microspheres (BGMs) with well-characterised external surfaces offer better-controlled ion release kinetics and degradation rates. Moreover, the shape promotes a homogeneous microsphere distribution in cellular suspensions, enhancing cell adhesion [12]. Additionally, BGMs can be used for drug delivery systems and injectable materials in orthopaedic and dental applications. The uniform spherical shape and specific particle size range of BGMs enable precisely controlled and optimised ion dissolution [13–15].

Several procedures, including low- and high-temperature methods, have been applied to manufacture BGMs [12]. The low-temperature techniques are based on sol-gel processing [12,16]. However, the disadvantages of this method are high costs and limited yield [17]. One frequently used high-temperature method is flame-spraying, in which irregular bioactive glass particles are fed into a hot flame when they melt and form microspheres due to surface tension effects [16,18,19]. The rapid cooling after the flame prevents the crystallisation of the spheres. The flame-spraying parameters control the size and shape of the resulting spheres [13]. The separation of particles before entering the flame is a crucial criterion for obtaining dispersed homogeneous spheres. The residence time in the flame must be long enough to produce spheres also of the largest particles [11].

Commercial silicate-based bioactive glasses 45S5 and S53P4 are prone to crystallise during thermal processing [20,21]. Also, during the processing of the glass particles into amorphous spheres through flame

* Corresponding authors.
E-mail addresses: polina.sinitsyna@abo.fi (P. Sinitsyna), leena.hupa@abo.fi (L. Hupa).

https://doi.org/10.1016/j.jnoncrysol.2022.121736
Received 11 February 2022; Received in revised form 14 April 2022; Accepted 1 June 2022
Available online 11 June 2022

spheroidisation, the particles pass through the temperature ranges critical for crystallisation. The microspheres based on flame spheroidisation of 45S5 frits [22] and flame synthesis of alkali-activated 45S5 powder [17] yielded glass-ceramic microspheres containing $Na_2Ca_2Si_3O_9$ (combeite) crystals.

Brink et al. studied whether adding K_2O, MgO and B_2O_3 increases the thermal processing window of silicate-based bioactive glasses [23]. Glass 13–93 (in wt.%: 53 SiO_2, 6 Na_2O, 12 K_2O, 5 MgO, 20 CaO, 4 P_2O_5) one of the 40 statistically selected compositions studied, showed the desired *in vivo* bioactivity and could be sintered into porous bodies and drawn into continuous fibres [23–25]. Brink et al. successfully produced 13–93 BGMs through spheroidisation in a flame [26]. The diameter of the 13–93 BGMs varied from 74 to 297 μm. 13–93 BGMs showed similar dissolution behaviour in tris(hydroxymethyl)aminomethane (TRIS) as the crushed particles before the spheroidisation, thus verifying that the short residence time in the high flame temperature did not affect the bioactivity of 13–93. Later, porous scaffolds sintered of the flame-sprayed 13–93 microspheres were shown to bond and regenerate bone tissue [27].

Bioactive glass 13–93 has been approved for *in vivo* use in Europe [28]. Another silicate-based bioactive glass, S53P4 (wt.%: 53 SiO_2, 23 Na_2O, 20 CaO, 4 P_2O_5), is approved by the EU (CE marking) and the US Food and Drug Administration (FDA) for orthopaedic use. S53P4, commercially available as Bonalive®, is also reported to provide antibacterial effects and inhibit bacterial growth [29–31]. The bone regenerative performance of a commercial putty consisting of S53P4 microspheres (12 wt.% 90–425 μm) and S53P4 granules (48 wt.% 500–800 μm) in a synthetic binder mixture of glycerol and polyethene glycols was studied in rabbit tibia defect [32]. The putty provided reliable bone regeneration without adverse tissue or cellular reactions.

Our recent study reported ion release from commercial S53P4 microspheres under static and dynamic conditions in TRIS and simulated body fluid (SBF) [33]. The microsphere composition markedly deviated from the nominal glass depending on the sphere size: the smaller the spheres, the lower the Na_2O and P_2O_5 content in the BGMs. The results suggested that the conditions in the flame seem to turn the smaller particles into spheres that dissolve only slowly *in vitro*.

The present work aimed to optimise the flame-spraying parameters for processing S53P4 BGMs with the chemical composition corresponding to the nominal glass in laboratory conditions. The focus was on the smaller microsphere fractions (45–125 μm) for detailed dissolution kinetic studies under a dynamic environment. These tiny microspheres are for interest, e.g., as rapidly dissolving components to provide antimicrobial effects to putties consisting of larger BGMs. 13–93 BGMs were used as a reference for better understanding the impact of the flame-spraying on the composition, surface morphology, dissolution behaviour, and *in vitro* bioactivity of the flame-sprayed microspheres.

2. Materials and methods

2.1. Microsphere synthesis

Two bioactive silicate glasses, i.e. S53P4 and 13–93, were melted from batches mixed from analytical grade reagents: Na_2CO_3, K_2CO_3, MgO, $CaCO_3$, $CaHPO_4{\cdot}2(H_2O)$ and Belgian quartz sand as the SiO_2 raw material. The glasses were melted in a platinum crucible at 1360 °C for 3 h, then cast, and annealed at 520 °C for 1 h. The glasses were crushed and remelted to ensure homogeneity. The annealed glass bars were crushed and sieved for future characterisation to obtain two narrow, well-defined particle size fractions of 45–90 μm and 90–125 μm. The particles were processed into microspheres via flame-spraying as described below. Similar method has been applied in many studies [19, 26,34-38].

The microspheres were produced in an in-house developed high-temperature laboratory-scale reactor made of stainless steel (Fig. 1). Crushed glass particles of the bioactive glasses S53P4 and 13–93 were fed manually (approximately 0.1 g/s) to a propane burner via a ceramic feeding tube. The burner and fuel type (propane) were selected to obtain the appropriate flame characteristics (stability, temperature, residence time) needed for the tests. The propane flow was around 5 kg/h, and the flame temperature was about 1900 °C. The inner diameter of the ceramic feeding tube was 1.5 cm. The length of the stainless steel tube was 0.7 m, and the diameter was 0.5 m. The length of the flame was approximately 0.5 m. The crushed particles were rapidly heated after entering the flame and rapidly cooled when leaving the flame, forming microspheres that were collected at the bottom of the stainless steel tube after the experiments. After leaving the flame, the particles are naturally cooled by convection, radiation, and heat transfer to the stainless steel surface after colliding with the surface. The cooling rate can be estimated based on approximate values for the cooling (1000 K in <100 ms), to a cooling rate of 10000 K/s. It can be expected that too high flame temperature and too long residence times (defined partly by the flow rates) cause the release of more volatile elements such as Na and P, although a sufficiently high temperature is needed in order to obtain spheroidisation. Typically, one experiment lasted for around 1 min.

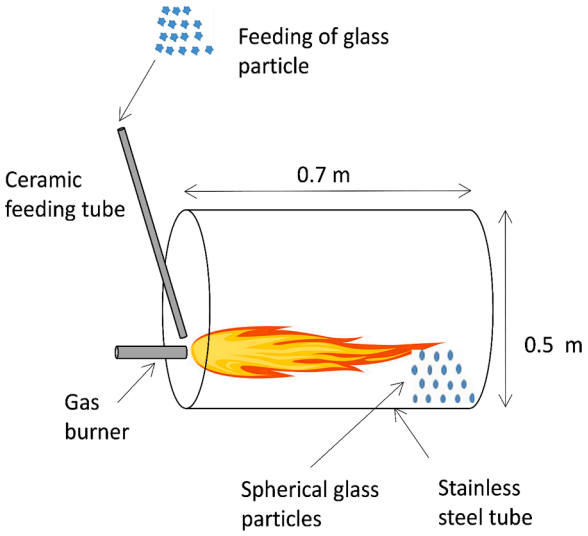

Fig. 1. Laboratory-scale reactor setup for manufacturing of flame-sprayed microspheres.

2.2. Characterisation of microspheres

2.2.1. Differential thermal analysis (DTA)

The thermal properties indicating the glass transition temperature T_g and crystallisation peak temperature T_p of the microspheres were determined using DTA (Netzsch STA 449F1). Fine powder (<45 μm, 10 mg) of milled BGMs were heated in platinum pans in N_2 atmosphere to 1100 °C (S53P4) and 1300 °C (13–93) with a heating rate of 10°C/min.

2.2.2. Morphology, composition, and size distribution

The surface morphology and composition of the microspheres were studied using scanning electron microscopy (SEM, Leo 1530, Oberkochen, Germany), equipped with an energy-dispersive X-ray analysis (EDXA, Thermo Scientific UltraDry, Thermo Scientific, Madison WI). After the *in vitro* dissolution in TRIS and SBF, the sphere surface composition was analysed from the cross-sections. Before the analysis, the samples were dried at 37 °C, embedded into epoxy resin, and polished to reveal the cross-section areas.

The size fractions and distribution of the microspheres were measured several times per sample using a laser diffraction system (Malvern Pananalytical Mastersizer 3000) controlled with the Malvern Instruments software (v3.63).

2.2.3. Microsphere phase composition

The amorphous nature of the microspheres was verified with X-ray diffraction (XRD, Empyrean Malvern Panalytical, Almelo, Netherlands) with the radiation source α-line of Cu radiation with the step size 2.0°/min at 40 mA, 40 kV, 2Θ range from 10° to 70°.

2.2.4. Glass structure and reaction layers

The glass structure and reaction layer formation before and after the dissolution of S53P4 and 13–93 microspheres in SBF were characterised with Fourier-transform infrared spectroscopy (FTIR) using a Harrick's Video-MVP™ ATR accessory. The ATR accessory was attached to a Bruker IFS 66S spectrometer equipped with a DTGS detector. The spectra were collected for the range 4000 to 400 cm^{-1} using a resolution of 4 cm^{-1}.

2.3. In vitro dynamic dissolution

The dissolution and bioactivity of microspheres were studied in dynamic flows of TRIS and SBF for 72 h at 37 °C. SBF was prepared according to the instructions by Kokubo et al. [39]. The 50 mM TRIS buffer was prepared by dissolving 12 g tris(hydroxymethyl)aminomethane in 1600 mL deionised water and heating at 37 °C for 3 h in water bath. 1 M HCl was used to adjust the initial pH of the solutions to 7.4. The experiments were performed in a continuous flow-through reactor set-up described in detail by Fagerlund et al. [33,40]. 210±5 mg of microspheres was weighed in the sample cell. The *in vitro* solutions were fed through the samples using a 0.2 mL/min rate to provide a laminar flow (Re < 2300). The solutions were collected after the reactor for different periods to measure the pH and analyse the concentration of ions released from the microspheres. The ions were analysed with inductively coupled plasma atomic emission spectroscopy (ICP-OES) (Optima 5300 DV, PerkinElmer). Separate dissolution runs were performed to collect the microspheres for SEM-EDX, FTIR and XRD analyses at 8, 24, and 72 h.

3. Results

3.1. Microsphere composition and size distribution

Fig. 2 shows an SEM image of flame-sprayed S53P4 microspheres of the size fraction of 45–125 μm. S53P4 granules and BGMs oxide compositions (in wt.%, and mol.%) were verified via EDX analysis (Table 1). The slight differences between the nominal analysed compositions suggest that the flame-spraying did not notably affect the BGMs composition. In our previous work, only the largest commercial S53P4 BGMs (diameter > 300 μm) had a composition close to the nominal glass [33]. In contrast, the number of spheres with a low content of Na_2O and P_2O_5 increased with decreasing sphere size. The BGMs composition in this work implies that the flame temperature was high enough to soften the glass to enable sphere formation. Further, the granule residence time

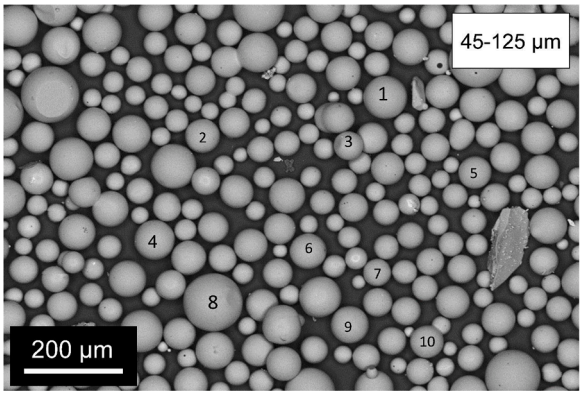

Fig. 2. SEM image of flame-sprayed 45–125 μm S53P4 BGMs.

Table 1
Oxide composition of S53P4 microspheres in wt.% (mol.%). The nominal and analysed average composition of the granules before flame-spraying are also given.

S53P4 Microsphere nr	Oxide content, wt.% (mol.%)			
	Na_2O	SiO_2	P_2O_5	CaO
Nominal	23.0 (22.7)	53.0 (53.9)	4.0 (1.7)	20.0 (21.8)
1	25.9 (25.7)	50.2 (51.1)	4.1 (1.7)	19.8 (21.5)
2	26.3 (25.9)	51.2 (52.1)	3.7 (1.7)	18.8 (20.5)
3	26.7 (26.6)	49.8 (50.6)	3.7 (1.6)	19.8 (21.3)
4	27.1 (26.7)	49.6 (50.4)	3.8 (1.6)	19.5 (21.2)
5	27.3 (26.9)	49.3 (50.1)	3.6 (1.5)	19.8 (21.5)
6	26.8 (26.5)	51.1 (51.9)	3.6 (1.5)	18.5 (20.1)
7	26.9 (26.5)	49.2 (50.0)	3.9 (1.7)	20.0 (21.8)
8	25.4 (25.0)	51.1 (52.0)	4.0 (1.7)	19.5 (21.3)
9	26.9 (26.5)	49.2 (50.0)	3.6 (1.5)	20.3 (22.0)
10	27.1 (26.7)	49.8 (50.6)	3.8 (1.6)	19.3 (21.1)
Average ± SD	**26.6 ±0.6 (26.3±0.6)**	**50±0.8 (50.9±0.8)**	**3.8±0.2 (1.6±0.1)**	**19.5±0.5 (21.2±0.6)**
Granules (Average ± SD)	25 ±0.6 (24.6 ±0.6)	51±0.7 (51.7±0.7)	3.5 ±0.2 (1.5±0.1)	20.4 ±0.4 (22.1±0.5)

in the flame was short enough not to lead to the volatilisation of elements such as Na and P from the spheres. These results are in line with Lakhkar et al., who flame-sprayed titanium phosphate glass microspheres of the size range of 63–106 μm [19].

SEM images of flame-sprayed 13–93 microspheres of size fractions 45–90 and 90–125 μm are given in Fig. 3. The oxide compositions of the granules before entering flame-spraying (in wt.%, and mol.%) are shown in Table 2. No significant composition differences were observed between the granules and BGMs of this reference glass with a wide working range [25,26].

Fig. 4 gives the size distribution of the flame-sprayed S53P4 and 13–93 BGMs. The mean diameter was 67 μm for S53P4 and 75 μm for 13–93. For the size fraction of 90–125 μm, the mean diameter was 110 μm for both glasses. The size distributions for the two narrow sphere size fractions differ: the size distribution of the larger microspheres is broader with spheres ranging from 50 to more than 200 μm. Nevertheless, most sphere's size is close to the average particle size for both BGMs. As spheres in both size fractions had a composition close to the nominal glasses S53P4 and 13–93, these fractions are feasible materials in applications where rapid *in vivo* dissolution is desired.

The specific surface area of the BGMs was calculated according to Eq. (1)

$$SSA = \sum_x \frac{3}{r_x^* \rho} F_x \quad (1)$$

where SSA is the specific surface area given in m^2/g, ρ is the density of the glass (g/cm^3), r_x is the sphere radius (μm), and F_x gives the fraction of a specific particle size class on the volume basis. In the calculations, the reported density values 2.66 g/cm^3 for S53P4, and 2.76 g/cm^3 for 13–93 were utilised [41]. The calculated SSA for the smallest (45–90 μm) S53P4 spheres was 0.045 m^2/g, while for the 13–93, the calculated SSA was 0.029 m^2/g. For the size fraction of 90–125 μm, the differences

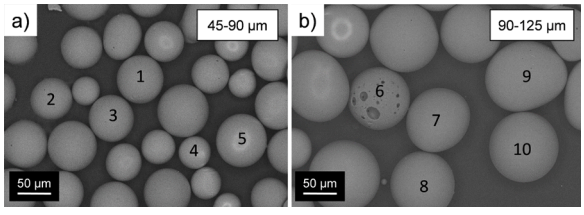

Fig. 3. SEM images of flame-sprayed 13–93 BGMs: (a) 45–90 μm; (b) 90–125 μm.

Table 2
Oxide composition of 13–93 granules and flame-sprayed 45–90 and 90–125 μm BGMs.

13–93 Microsphere nr	Oxide content, wt.% (mol.%)					
	Na_2O	SiO_2	P_2O_5	CaO	K_2O	MgO
Nominal	6.0 (6.0)	53.0 (54.6)	4.0 (1.7)	20 (22.1)	12 (7.9)	5 (7.7)
1	7.9 (7.9)	49.9 (51.7)	5.1 (2.2)	21.9 (24.3)	10.9 (7.2)	4.3 (6.6)
2	7.8 (7.8)	52.5 (54.3)	4.5 (2.0)	19.2 (21.7)	11.2 (7.4)	4.4 (6.8)
3	7.5 (7.5)	52.4 (54.4)	5.3 (2.3)	19.2 (21.4)	11.1 (7.4)	4.5 (7.0)
4	7.6 (7.6)	50.7 (52.5)	4.5 (2.0)	21.2 (23.5)	11.6 (7.7)	4.4 (6.8)
5	7.5 (7.5)	51.4 (53.1)	4.5 (2.0)	20.3 (22.5)	11.6 (7.6)	4.7 (7.2)
6	7.8 (7.9)	52.9 (55.0)	4.9 (2.2)	19.5 (21.6)	11.1 (7.4)	3.8 (5.9)
7	7.7 (7.7)	52.1 (53.8)	4.6 (2.0)	20.4 (22.6)	10.8 (7.1)	4.4 (6.8)
8	7.7 (7.7)	52.0 (53.7)	4.0 (2.0)	19.3 (21.8)	11.4 (7.5)	4.7 (7.2)
9	7.3 (7.3)	51.3 (53.2)	5.0 (2.2)	20.6 (22.9)	11.3 (7.5)	4.5 (7.0)
10	7.5 (7.5)	53.5 (55.5)	4.7 (2.1)	19.1 (21.2)	11.1 (7.3)	4.0 (6.3)
Average	**7.6 ±0.3 (7.6 ±0.2)**	**51.8 ±1.1 (53.7 ±1.8)**	**4.8 ±0.4 (2.3 ±0.3)**	**20.1 ±0.9 (22.3 ±1.1)**	**11.2 ±0.4 (7.4 ±0.3)**	**4.4 ±0.3 (6.6 ±0.6)**
13–93 granules (average)	6.6 (6.6)	53.3 (54.9)	3.9 (1.7)	20.4 (22.5)	11.4 (7.5)	4.4 (6.8)

in the calculated SSA was minor: 0.022 m^2/g for S53P4 and 0.020 m^2/g for 13–93 spheres. As expected, the larger the particle size, the lower the SSA.

3.2. Thermal properties

Fig. 5 shows the thermal properties of crushed BGMs. The inflection point of the endothermic peak starting at around 500 °C was taken as the glass transition temperature T_g, suggesting 550 °C for S53P4 and 595 °C for 13–93. In general, the measured T_g values for S53P4 and 13–93 BGMs were similar as reported for the glasses before flame spheroidisation [42,43]. In accordance with the literature, the crystallisation of S53P4 started at 650 °C, i.e. the commencement of the endothermic peak [44,45]. The crystallisation peak temperature (T_p) for S53P4 was 747 °C, while for 13–93, the peak was 933 °C. Due to its wide working range, defined as the temperature window between T_g and T_x, 13–93 has been frequently utilised for developing various hot-worked amorphous structures of bioactive glasses, e.g. fibre drawing, sintering of porous bodies or additive manufacture followed by sintering [46].

3.3. Changes in the solution pH and ion concentrations

The pH changes during the dynamic dissolution of S53P4 (a) and 13–93 (b) BGMs in TRIS and SBF were measured up to 72 h (Fig. 6). The pH of the outflow solutions from the reactor containing S53P4 spheres showed an initial increase but decreased to values close to inflow solution pH. Thus, the ion concentrations released from the gradually dissolving microspheres were not high enough to increase the pH of the fresh flows of the buffered solutions. For 13–93, the pH trends implement similar changes in TRIS and SBF, while smaller particles provided higher pH values. The 13–93 BGMs dissolution in TRIS led to slightly higher values than S53P4 BGMs. After 24 h of dissolution, the pH values of TRIS and SBF were similar for both S53P4 BGMs fractions.

The ion concentrations in TRIS and SBF after the dissolution of S53P4 BGMs are presented in Fig. 7. Higher Ca concentrations were released into TRIS than SBF (Fig. 7a). Also, the concentration was less after 72 h in SBF than in the original solution, thus suggesting precipitation of the calcium compounds. Ca and Na showed identical dissolution patterns in TRIS for the two S53P4 BGMs size fractions (Fig. 7a and b). Na release into SBF is not shown as the solution's high initial content (3410 mg Na/l) challenges accurate analysis. The initial Si release from both BGMs

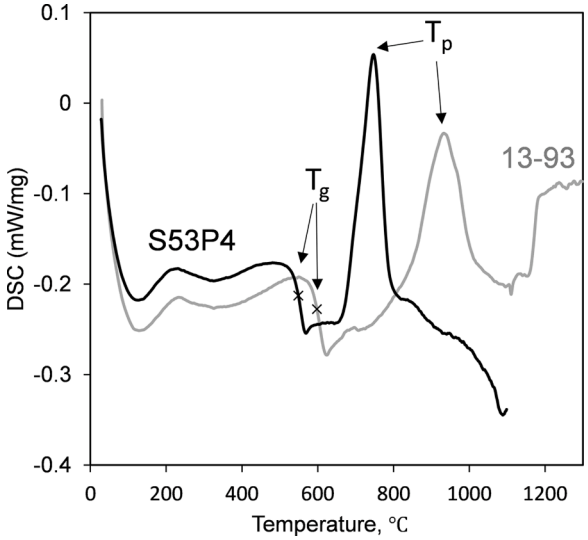

Fig. 5. DTA of powdered S53P4 and 13–93 BGMs.

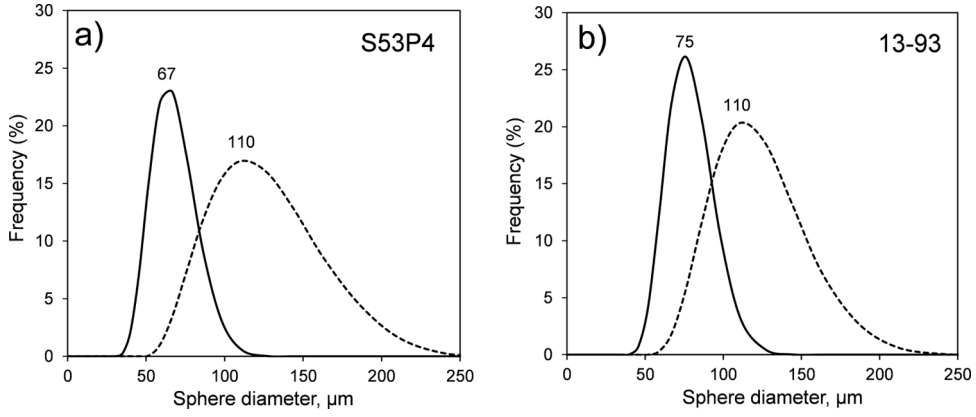

Fig. 4. Sphere size distribution of the 45–90 μm and 90–125 μm flame-sprayed BGMs: (a) S53P4; (b) 13–93.

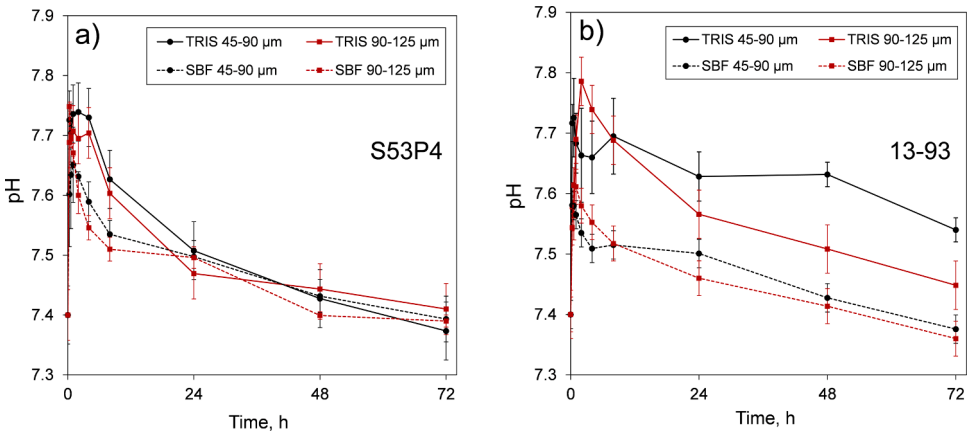

Fig. 6. pH changes of TRIS and SBF as a function of time for 45–90 µm and 90–125 µm BGMs: (a) S53P4 and (b) 13–93.

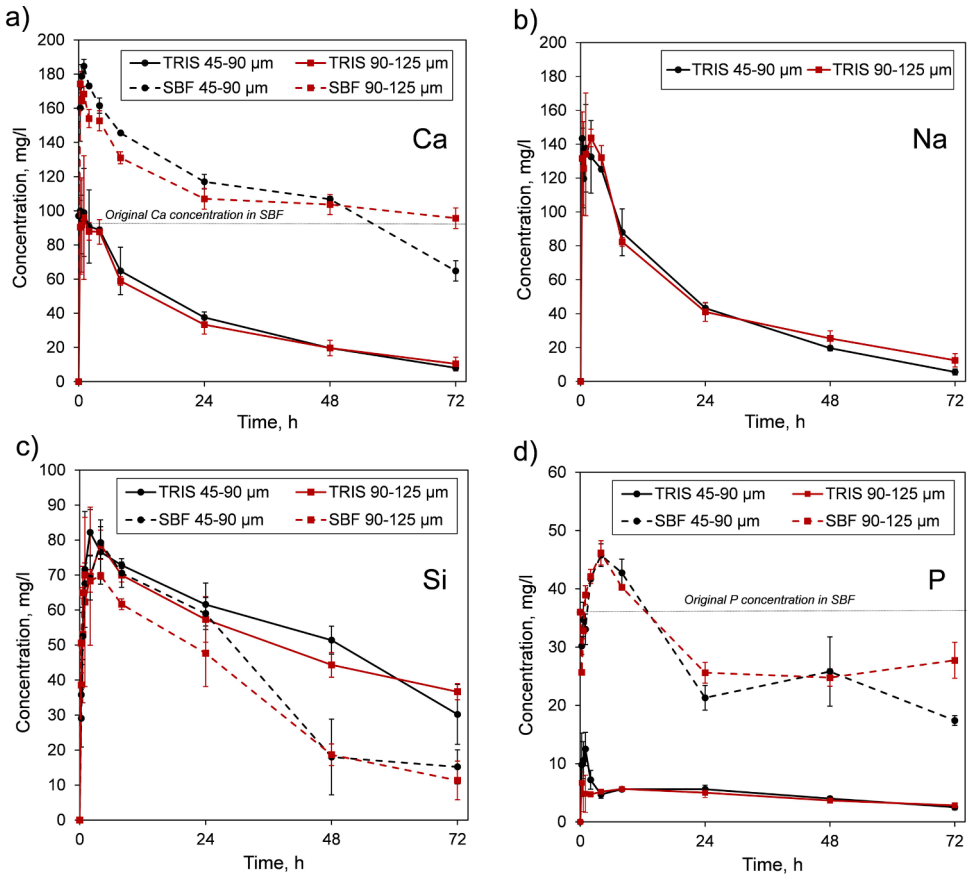

Fig. 7. Ion dissolution profiles of S53P4 BGMs in TRIS and SBF.

fractions was similar in SBF and TRIS (Fig. 7c). During the first hours, the Si concentration in TRIS increased to about 80 mg/L for both S53P4 sphere fractions and then steadily decreased to around 40 mg/L at 72 h. However, Si concentrations were lower in SBF than in TRIS at longer dissolution times. Moreover, the P concentration changes were bigger in SBF compared to TRIS (Fig. 7d).

Fig. 8 gives ion concentrations in solutions after the dissolution of 13–93 BGMs in TRIS and SBF. The concentrations of all ions released into TRIS were slightly higher for the 45–90 µm spheres than the 90–125 µm spheres. The release of Ca and Mg into the two solutions showed similar patterns, i.e. a steady decrease after an initial peak (Fig. 8a and d). For a more precise comparison of the alkali ions released from S53P4 and 13–93 BGMs into TRIS, the ion concentrations were converted into mol/L. After 24 h of dissolution in TRIS, the molar amount of Na released from the smallest S53P4 spheres was 1.9 mol/L compared to 1.5 mol/L of Na+K from the 13–93 spheres. For the 90–125 µm spheres, the calculated values at 24 h were slightly lower: 1.8 mol/L of Na for S53P4 compared to 1.2 mol/L of Na+K for 13–93. This comparison suggests that the molar amount of Na released from the S53P4 spheres was higher than the total molar amount of Na+K released from the 13–93 spheres. The Si release trends from 13 to 93 into the two solutions were similar to S53P4, i.e. minor differences between the solutions during the first hours, but then higher release into TRIS (Fig. 8e).

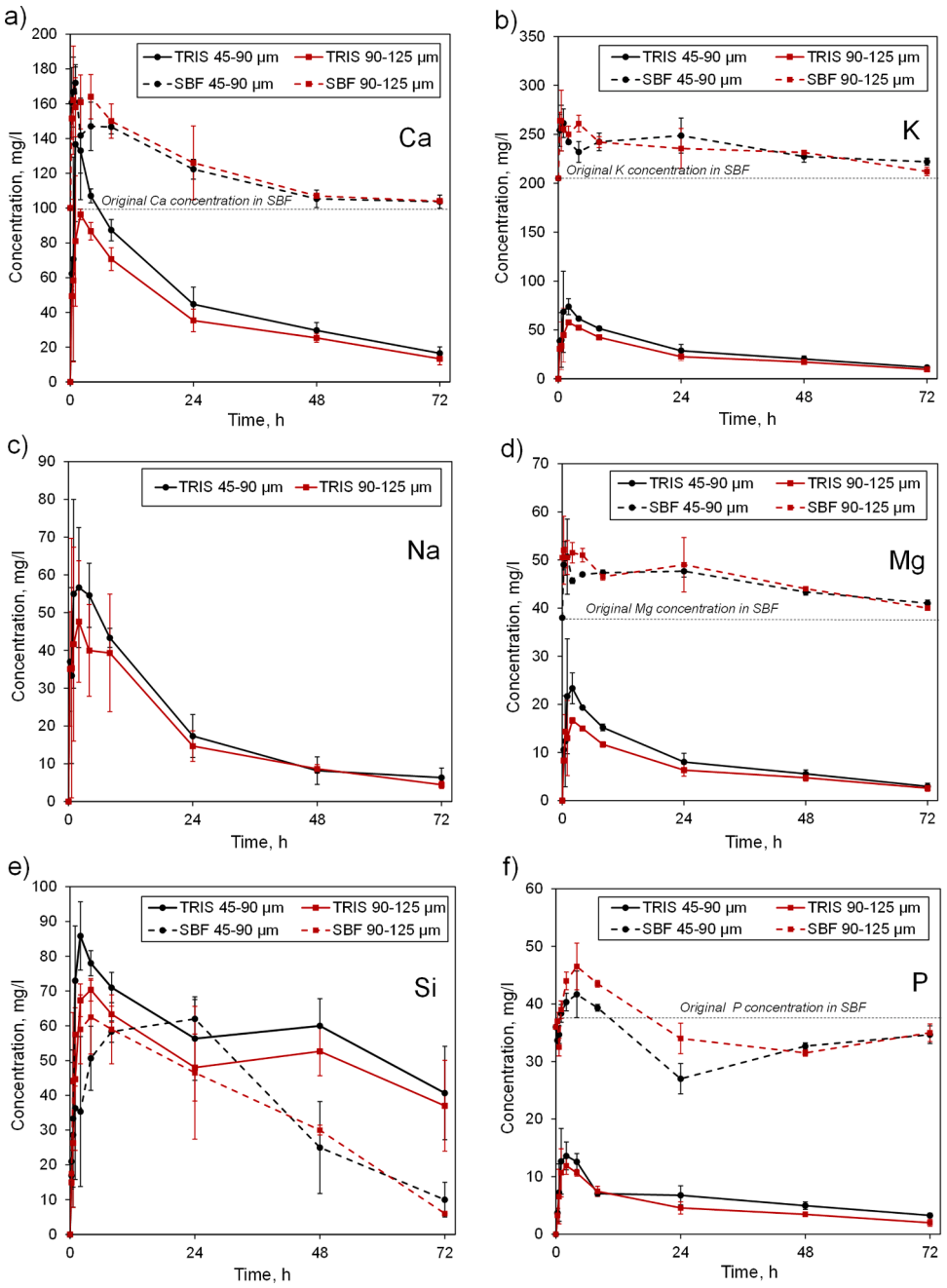

Fig. 8. Ion dissolution profiles of 13–93 BGMs in dynamic TRIS and SBF.

3.4. Microsphere surface composition

The FTIR spectra of S53P4 and 13–93 BGMs before and after 8, 24, and 72 h of dissolution in SBF are given in Fig. 9. The spectra show asymmetric stretching of Si-O vibrations for bridging oxygen (Si-O BO) at 1030 cm^{-1} and Si-O for non-bridging oxygen stretching (Si-O NBO) at ~ 923 cm^{-1} [47]. These vibrations confirm the incorporation of alkalis (Na and K) and alkaline earths (Ca and Mg) in the glass network, and also K and Mg in the 13–93 network [16]. For both size fractions of S53P4 BGMs, the bands at 605 cm^{-1} provided vibrations already after 8 h, while these vibrations were visible for 13–93 spheres only after 72 h. After 72 h of dissolution in SBF, all microspheres exhibited bands at 605 cm^{-1} and 560–565 cm^{-1}, which can be attributed to the asymmetric bending vibrations of PO_4^{3-}, indicating CaP formation [48]. FTIR results imply that the CaP layer formed more slowly on 13–93 than S53P4 spheres.

XRD patterns of S53P4 and 13–93 BGMs before and after 8, 24, and 72 h of dissolution in SBF are shown in Fig. 10. Microspheres of both glasses were amorphous before the dissolution experiments. Further, the peaks at 26° and 32° verify hydroxyapatite (HA, $Ca_{10}(PO_4)_6(OH)_2$) on both S53P4 and 13–93 BGMs after 72 h of dissolution in SBF [49].

3.5. In vitro bioactivity

Fig. 11 shows cross-sections of both S53P4 and 13–93 BGMs fractions after 72 h of dissolution in SBF. Silica-rich (darker grew layer) and CaP (light grey outer layer) had formed at the microsphere surface. The CaP layer thickness was higher for the larger BGMs. In addition, the EDX line-analyses along with the arrows in Fig. 12 also suggest that the Ca and P contents (in wt.%) were slightly higher for the larger spheres (90–125 µm). Based on the EDX results, the calculated Ca/P ratios were 1.42 for the 45–90 µm and 1.51 for the 90–125 µm S53P4 BGMs. For

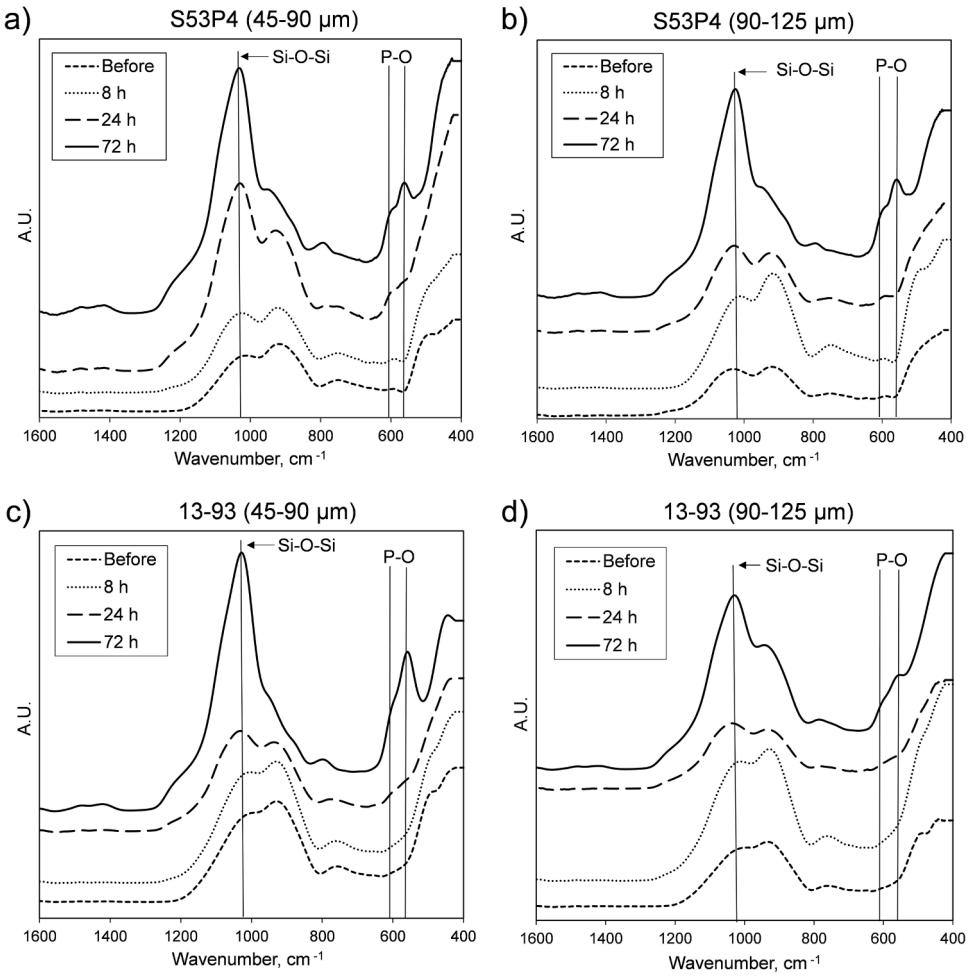

Fig. 9. FTIR spectra of S53P4 and 13–93 BGMs before and after the dynamic dissolution in SBF.

13–93, the Ca/P ratios were 1.33 for the fraction 45–90 µm and 1.38 for the fraction 90–125 µm.

Fig. 13 shows the cross-sections of S53P4 BGMs for the size fraction of 90–125 µm after 8, 24, and 72 h of dissolution in TRIS and SBF. Si-rich layers were observed after 8 h of dissolution in both solutions. The reaction layer thicknesses for BGMs increased with dissolution time in both solutions. Further, after 8 h in SBF, a CaP layer with a thickness of around 1 µm was identified at BGMs. The layer thickness increased with time and was 5 µm after 72 h. For the smallest S53P4 BGMs, no CaP layer was detected at the microsphere surfaces after 8 h of dissolution in TRIS and SBF (not shown here).

Fig. 14 shows SEM images of S53P4 and 13–93 BGMs cross-sections after 72 h of dissolution in TRIS. Differences between the silica-rich and CaP layer thicknesses can be seen between the two size fractions of S53P4 spheres. For S53P4 microspheres, the Si-rich layer thicknesses were from 8 to around 16 µm for 45–90 µm fraction, and 10–25 µm for 90–125 µm fraction. The CaP layer thicknesses were 1–2 µm for 45–90 µm, and around 2 µm for 90–125 µm spheres. For 13–93, the silica-rich layer was slightly thicker for the larger spheres: around 20 µm compared to 10–15 µm for the smallest spheres. The SEM micrographs (Fig. 14) also indicate the formation of only mixed silica and CaP (Si+CaP) layer after 72 h of dissolution of both fractions of 13–93 microspheres in TRIS. The EDX analysis of the mixed Si+CaP layer for 13–93 microspheres is also included in the figure.

4. Discussion

4.1. Dynamic dissolution of microspheres

The dissolution of S53P4 and 13–93 microspheres followed the bioactive glass reactions suggested by Hench et al. [9]. The initial pH increase can be explained by the ion-exchange reaction between Ca^{2+} and Na^{+} in the glass and protons in the solution. The higher pH and thus higher dissolution were assumed to be mainly due to 13–93 containing two alkalis, Na_2O and K_2O, while only Na_2O is present in S53P4. Potassium has weaker bonding to the glass network compared to sodium, thus dissolving easier [50,51]. The lower molar amount of Na+K released from the 13–93 spheres compared to S53P4 suggests that the observed higher pH of TRIS in the dissolution of 13–93 (Fig. 6) most likely was not due to enhanced release of total alkalis from 13 to 93, but the overall differences in the oxide composition of the two glasses. The higher ion release of the smallest 13–93 spheres into TRIS is correlated to the higher specific surface area, and thus faster reaction rates. The initial increase of Si concentration for the two fractions of S53P4 and 13–93 BGMs can be attributed to the initial pH increase followed by a decrease of Si concentration due to the formation of silica-rich and CaP reaction layers at the BGMs. The high surface areas of the S53P4 and 13–93 microspheres are of interest in applications where a high initial release of ions is desired, e.g., for antibacterial effect in an implanted cavity. However, the impact of all the ions released on other cellular processes must be known to better evaluate the suitability of the tiny microspheres in a particular application. The changes in the P concentrations in TRIS and SBF were in line with the changes in the alkali earth

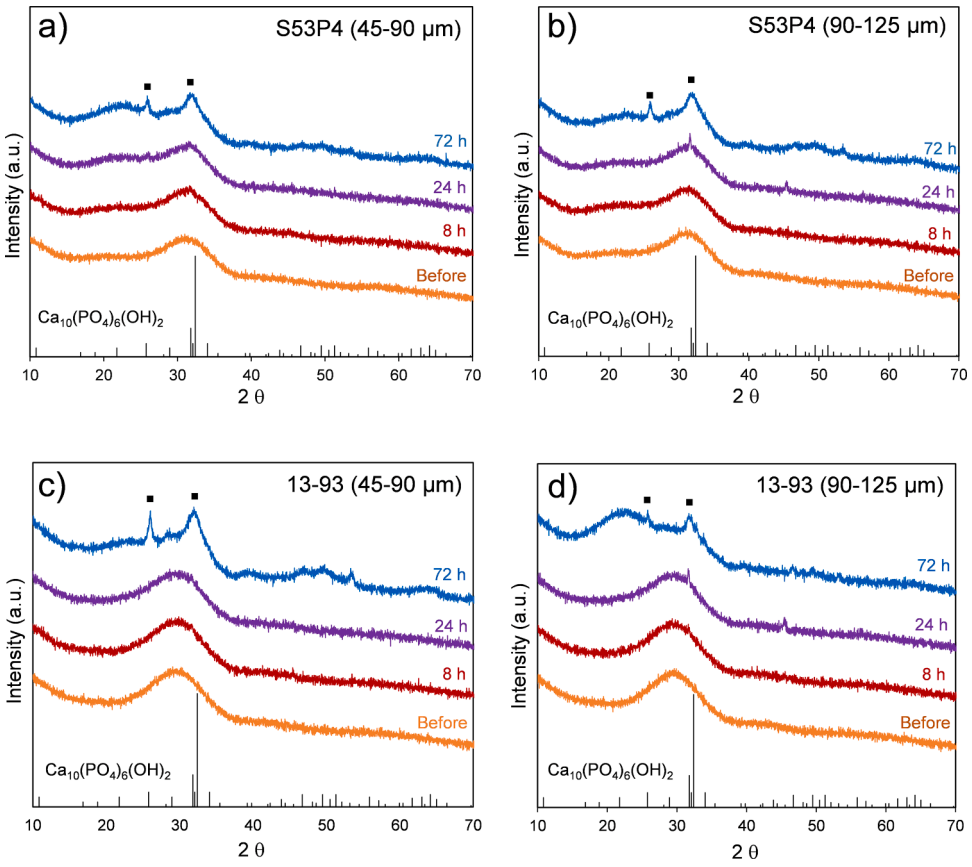

Fig. 10. XRD patterns of S53P4 and 13–93 BGMs before and after the dynamic dissolution in SBF.

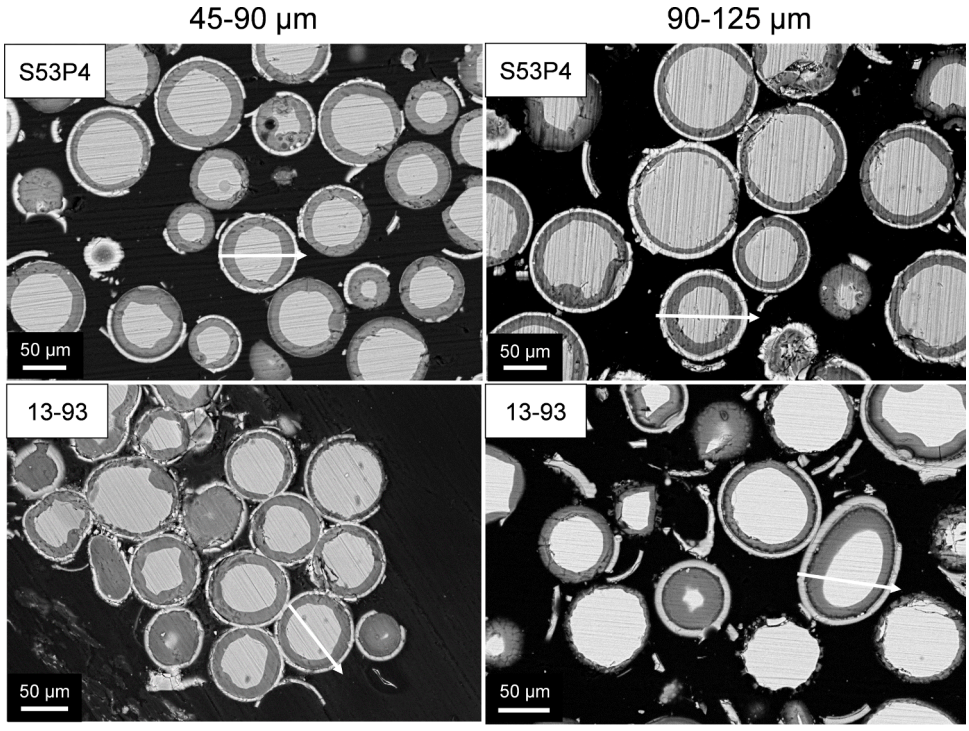

Fig. 11. SEM images of S53P4 and 13–93 BGM cross-sections after 72 h of dissolution in SBF.

ion concentrations, thus suggesting precipitation of phosphate species. However, the lower phosphate concentration decrease suggested less CaP or HA on 13–93 than S53P4. The differences in the pH of SBF upon dissolution of both BGMs compositions were in line with the results by Zhang et al. for 500–800 μm particles of the same glasses [52]. They reported higher pH for S53P4 than 13–93 in circulated SBF. However, in

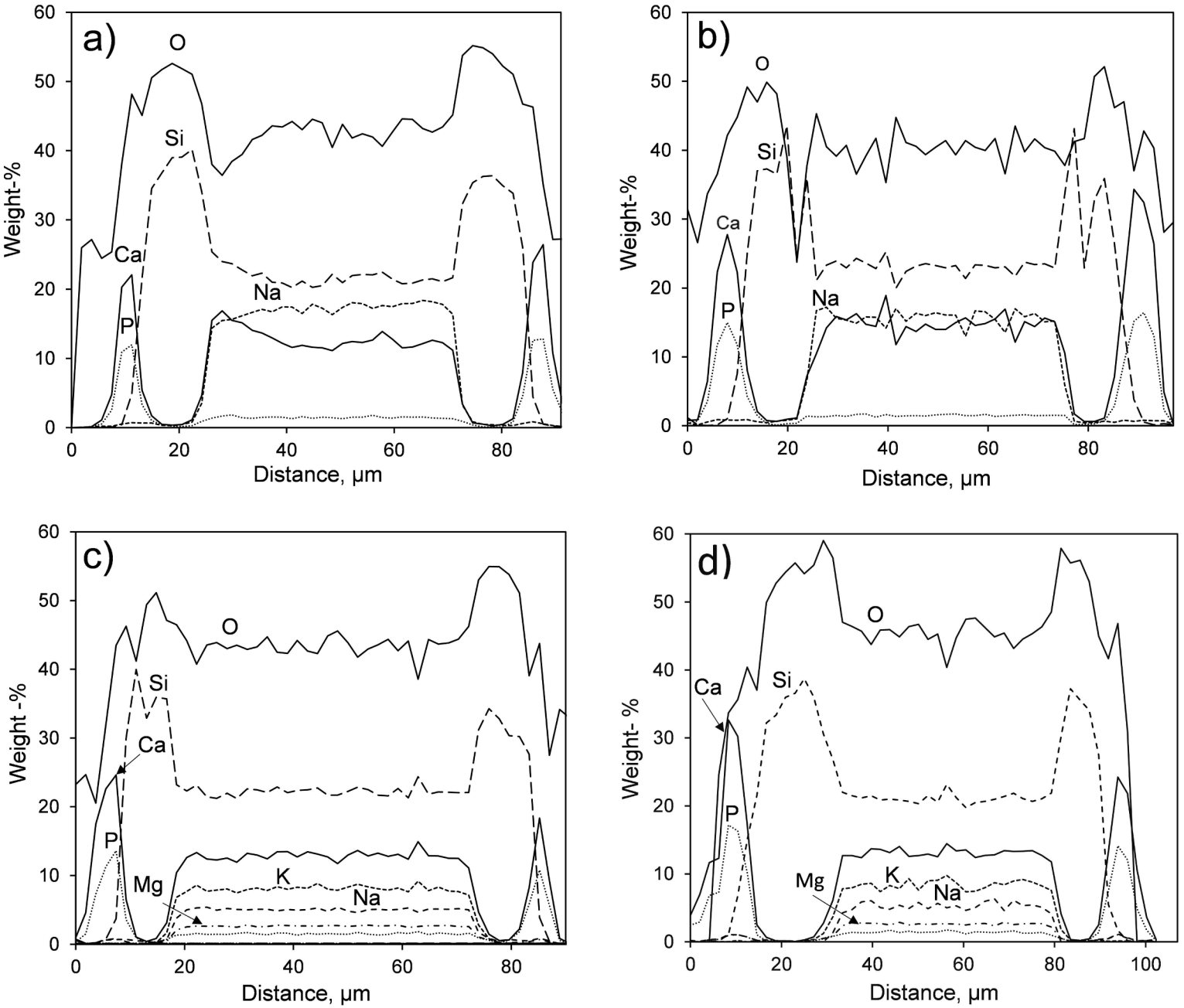

Fig. 12. EDX line analysis of S53P4 BGMs: 45–90 μm (a), 90–125 μm (b), and 13–93 BGMs: 45–90 μm (c), 90–125 μm (d) along the arrows in Fig. 11.

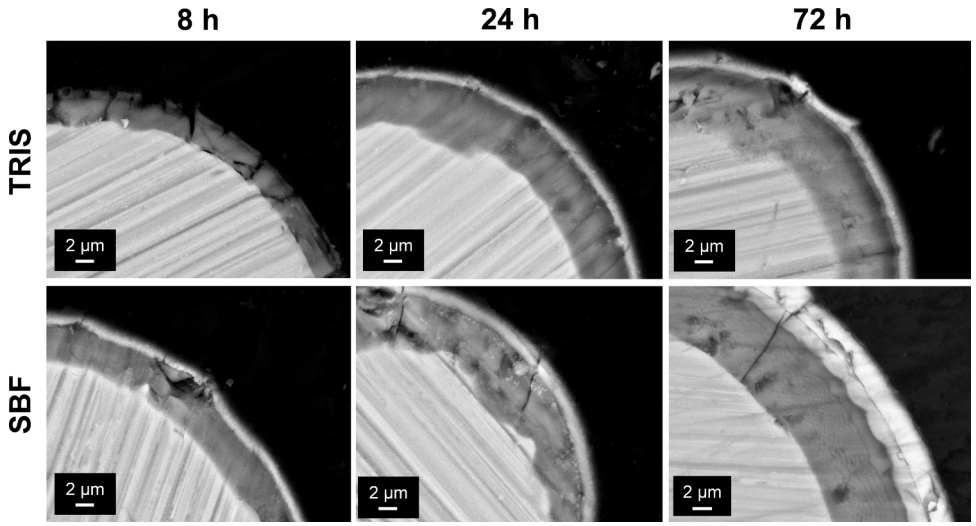

Fig. 13. SEM images of S53P4 (90–125 μm) BGMs cross-sections after 8, 24 and 72 h of dynamic dissolution in TRIS and SBF.

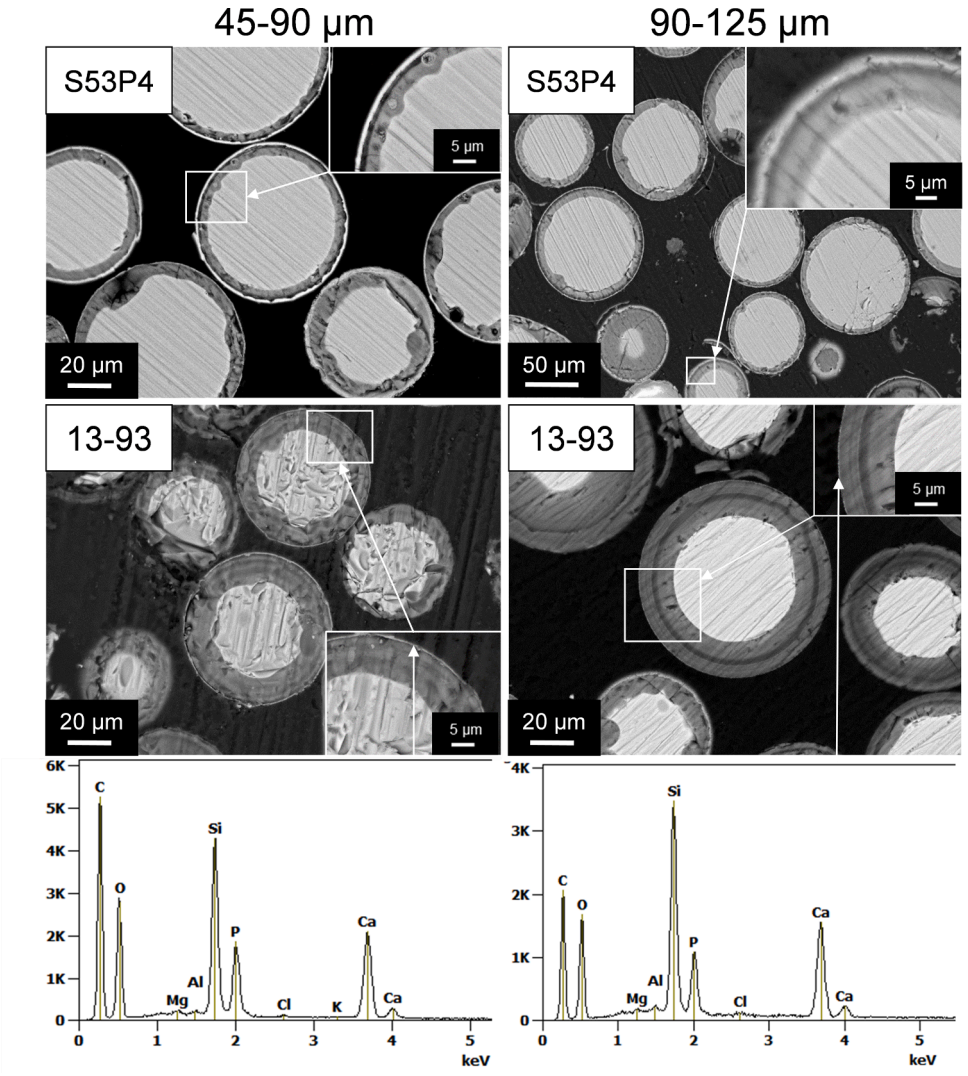

Fig. 14. SEM images of cross-sections of 45–90 and 90–125 μm S53P4, and 13–93 BGMs after 72 h of dynamic dissolution in TRIS. The EDX analysis shows mixed Si+CaP layer formation on the surface of both fractions of 13–93 spheres.

this work, the pH gradually decreased after the initial release due to the fresh fluid flow feed compared to the specific fluid volume circulated in the experiments by Zhang et al. Moreover, the decrease of pH can be explained by the lower mass of microspheres left in the reactor after continuous flow-through dissolution. For example, the mass loss for the smallest S53P4 microspheres was around 90% after 72 h of dissolution in TRIS. The lower release of Si into SBF was assumed to depend on the formation of thicker CaP surface layers in SBF, thus acting as a dissolution barrier of the glasses. Ca and P concentrations increased in SBF for both fractions of S53P4 and 13–93 microspheres, and then gradually decreased due to the formation of a CaP layer as reported for the granules of these two glasses [53].

4.2. Effect of the microsphere size on layer formation

The dissolution of BGMs directly correlated to their sphere size range, indicating that the dissolution rate increased as the sphere size decreased and, consequently, the surface area increased [54]. The CaP layer results from several reaction steps at the glass surface. In general, higher dissolution rates result in higher concentrations of dissolved Ca and P ions in the solution. Thus, more Ca and P species are available for CaP precipitation for the smaller particles. On the other hand, the formation of CaP depends on the availability of nucleation sites in the silica-rich layer, which are more available for larger particles than for smaller ones. Also, the higher total surface area of small particles requires higher Ca and P species concentrations for a certain CaP thickness. Greenspan et al. showed that smaller particles gave a faster release of ions but a less-developed CaP layer than larger particles with lower SA/V ratios [55]. Zhang et al. investigated the effect of particle size fraction on the reaction layer thickness as a function of dissolution time under static conditions [54]. Their results showed that larger particles had more distinct reaction layers than smaller fractions.

CaP layer identified after 24 h of dynamic dissolution in SBF could be correlated with the ion dissolution profiles of the microspheres (Figs. 7 and 8). Since the concentration of P increased during the first 2 h for the two S53P4 size fractions, the initial leaching was sufficient to support the formation of a distinct CaP layer at the BGMs. After 24 h, the P species concentration had decreased below the initial level in SBF for both fractions of S53P4 and 13–93 BGMs. In addition, the XRD results confirmed the presence of hydroxyapatite after 24 h for the larger (90–125 μm) S53P4 and 13–93 BGMs (Fig. 10), implying that hydroxyapatite formation was more significant on the larger spheres. The EDX analysis of the CaP layer gave a Ca/P-ratio that was closest to the stoichiometric HA ratio for the larger S53P4 microspheres. The atomic Ca/P ratio of the stoichiometric crystalline HA ($Ca_{10}(PO_4)_6(OH)_2$) is 1.67. According to the EDX analysis, the calculated Ca/P ratios were 1.35 and 1.39 for 45–90 μm and 90–125 μm spheres of S53P4 after 24 h in SBF. For 13–93, the ratios were 1.27 and 1.35 for 45–90 μm and 90–125 μm spheres, respectively. In our previous study, a thin CaP layer was identified on the surface of the largest (300–500 μm) commercial S53P4 BGMs after 72 h of static and dynamic dissolution in TRIS and SBF [33]. After 24 h in TRIS, a thin CaP layer was identified on the S53P4 microspheres in the present work. The difference in reaction layer formation ability between S53P4 and 13–93 BGMs can also be explained by the presence of magnesium in the 13–93 composition, which reduces the bioactivity [56]. Fagerlund et al. reported that only sporadic CaP layers were identified for 13–93 compared to 45S5 and S53P4 granules after 120 h of static dissolution in TRIS [53]. Moreover, Cacaina et al. did not observe any CaP layer at the surface of 125–250 μm 13–93 microspheres after 27 days of static dissolution in TRIS [34].

Tiny microspheres were successfully flame spheroidised from the particles of bioactive glasses S53P4 and 13–93 without any measurable alkali or phosphorus volatilisation. Whether similar tiny microspheres could be manufactured from bioactive glasses with lower SiO_2 contents has to be studied separately. Most likely, both alkali volatilisation and particle crystallisation will challenge the spheroidisation. The ion dissolution trends and evolution of silica-rich and hydroxyapatite reaction layers at the microspheres were comparable with findings reported for the particles of the same glasses. Thus, the S53P4 microsphere processing through flame spheroidisation was successful. The microspheres can potentially be utilised for new products based on the S53P4 bioactive glass. In addition, the results provide a basis for more theoretical studies of glass dissolution.

5. Conclusions

S53P4 and 13–93 BGMs with the size fractions of 45–90 and 90–125 μm were successfully produced using the flame-spraying method. According to EDX results, the oxide composition of the produced microspheres was close to the nominal. The pH and ion concentration profiles suggested that the microspheres gradually dissolved in SBF and TRIS. After 8 h of dissolution in SBF, a CaP layer was observed at the external surface area of the S53P4 microspheres. The layer thickness increased with dissolution time and was more extensive for the larger spheres. Similar layers were formed in TRIS on S53P4 microspheres, but the CaP layer was observed later than in SBF. No distinct CaP layer formed in TRIS on the 13–93 microspheres, thus suggesting that released Ca and P concentrations were insufficient. In contrast, CaP was identified on 13–93 microspheres in SBF, indicating that the spheres provided suitable nucleation sites. SEM-EDX in combination with XRD analyses confirmed that the CaP layer at S53P4 and 13–93 BGMs had transformed into hydroxyapatite after 72 h of dissolution in SBF. The results verify that S53P4 microspheres have a similar reaction layer ability as irregular particles of the same glass. Thus, these BGMs have an excellent potential for injectable clinic products. The study shows that also tiny microspheres can be manufactured with flame-spraying without alkali volatilisation. The tiny microspheres can be mixed with large particles or spheres to enhance the antimicrobial properties of putties used as graft materials to threat cavities in bone tissue.

CRediT authorship contribution statement

Polina Sinitsyna: Conceptualization, Investigation, Methodology, Writing – original draft. **Oskar Karlström:** Investigation, Methodology, Writing – review & editing, Supervision. **Christoffer Sevonius:** Investigation. **Leena Hupa:** Conceptualization, Investigation, Methodology, Writing – review & editing, Supervision.

Declaration of Competing Interest

The authors declare that they have no known competing financial interests or personal relationships that could have appeared to influence the work reported in this paper.

Acknowledgments

This work was supported by the Graduate School of Chemical Engineering (GSCE) at Åbo Akademi University and the Academy of Finland (project no. 321598). This work was a part of the Business Finland project Biobased Smart Materials at Biomaterials Interface (project no. 8823/31/2019).

References

[1] L.L. Hench, The story of bioglass, J. Mater. Sci. Mater. Med. 17 (2006) 967–978, https://doi.org/10.1007/s10856-006-0432-z.
[2] L.L. Hench, Bioceramics, J. Am. Ceram. Soc. 81 (1998) 1705–1728, https://doi.org/10.1111/j.1151-2916.1998.tb02540.x.
[3] A. Hoppe, N.S. Güldal, A.R. Boccaccini, A review of the biological response to ionic dissolution products from bioactive glasses and glass-ceramics, Biomaterials 32 (2011) 2757–2774, https://doi.org/10.1016/j.biomaterials.2011.01.004.
[4] V. Miguez-Pacheco, L.L. Hench, A.R. Boccaccini, Bioactive glasses beyond bone and teeth–Emerging applications in contact with soft tissues, Acta Biomater. 13 (2015) 1–15, https://doi.org/10.1016/j.actbio.2014.11.004.

[5] V. Miguez-Pacheco, D. Greenspan, L.L. Hench, A.R. Boccaccini, Bioactive glasses in soft tissue repair, Am. Ceram. Soc. Bull. 94 (2015) 27–31, https://doi.org/10.1016/j.actbio.2014.11.004.

[6] F. Baino, S. Hamzehlou, S. Kargozar, Bioactive glasses: where are we and where are we going, J. Funct. Biomater. 9 (1) (2018) 25, https://doi.org/10.3390/jfb9010025.

[7] N.C. Lindfors, Clinical experience on bioactive glass S53P4 in reconstructive surgery in the upper extremity showing bone remodeling, vascularization, cartilage repair and antibacterial properties of S53P4, J. Botechnol. Biomater. 1 (2011) 111, https://doi.org/10.4172/2155-952X.1000111.

[8] K. Pernaa, I. Koski, K. Mattila, E. Gullichsen, J. Heikkilä, A.J. Aho, N.C. Lindfors, Bioactive glass S53P4 and autograft bone in treatment of depressed tibial plateau fractures: a prospective randomized 11-year follow-up, J. Long Term Eff. Med. Implant. 21 (2011) 139–148, https://doi.org/10.1615/jlongtermeffmedimplants.v21.i2.40.

[9] L.L. Hench, Ö.H. Andersson, An Introduction to Bioceramics. Advanced Series in Ceramics, World Scientific, Singapore, 1 (1993) 41–62. 10.1142/2028.

[10] Ö.H. Andersson, G. Liu, K.H. Karlsson, L. Niemi, J. Miettinen, J. Juhanoja, *In vivo* behaviour of glasses in the system Na_2O-K_2O-MgO-CaO-B_2O_3-P_2O_5-SiO_2, J. Mater. Sci. 1 (1990) 219–227, https://doi.org/10.1007/BF00701080.

[11] M. Brink, T. Turunen, R.P. Happonen, A. Yli-Urpo, Compositional dependence of bioactivity of glasses in the system Na_2O-K_2O-MgO-CaO-B_2O_3-P_2O_5-SiO_2, J. Biomed. Mater. Res. 37 (1997) 114–121, https://doi.org/10.1002/(SICI)1097-4636(199710)37:1<114::AID-JBM14>3.0.CO;2-G.

[12] K.M.Z. Hossain, U. Patel, I. Ahmed, Development of microspheres for biomedical applications: A review, Prog. Biomater. 4 (2015) 1–19, https://doi.org/10.1007/s40204-014-0033-8.

[13] L.E. Westerlund, M. Borden, Clinical experience with the use of a spherical bioactive glass putty for cervical and lumbar interbody fusion, J. Spine Surg. 6 (2020) 49–61, https://doi.org/10.21037/jss.2020.03.06.

[14] J.R. Jones, D. Brauer, L. Hupa, D.C. Greenspan, Bioglass and bioactive glasses and their impact on healthcare, Int. J. Appl. Glass Sci. 7 (2016) 423–434, https://doi.org/10.1111/ijag.12252.

[15] I. Saarenpää, J. Hirvoinen, J. Rinne, J. Frantzén, Novel bioactive glass putty (S53P4) as bone graft expander n minimally invasive lumbosacral interbody fusion, J. Minim. Invasive Spine Surg. Tech. 3 (2018) 52–58, https://doi.org/10.21182/jmisst.2018.00332.

[16] N.N. Gogajeh, J. Javadpour, B.E. Yekta, Low-temperature synthesis of bioactive glass-ceramic microspheres: Effect of processing temperature on the size and morphology, Ceram. Int. 47 (2021) 19895–19905, https://doi.org/10.1016/j.ceramint.2021.04.004.

[17] J. Kraxner, M. Michalek, A.R. Romero, H. Elsayed, E. Bernardo, A.R. Boccaccini, D. Galusek, Porous bioactive glass microspheres prepared by flame synthesis process, Mater. Lett. 256 (2019), 126625, https://doi.org/10.1016/j.matlet.2019.126625.

[18] M.B. Bortot, S. Prastalo, M. Prado, Production and characterization of glass microspheres for hepatic cancer treatment, Procedia Mater. Sci. 1 (2012) 351–358, https://doi.org/10.1016/j.mspro.2012.06.047.

[19] N.J. Lakhkar, J. Park, N.J. Mordan, V. Salih, L.B. Wall, H. Kim, S.P. King, J. V. Hanna, R.A. Martin, O. Addison, J.F.W. Mosselmans, J.C. Knowles, Titanium phosphate glass microspheres for bone tissue engineering, Acta Biomater. 8 (2012) 4181–4190, https://doi.org/10.1016/j.actbio.2012.07.023.

[20] S. Fagerlund, J. Massera, N. Moritz, L. Hupa, M. Hupa, Phase composition and *in vitro* bioactivity of porous implants made of bioactive glass S53P4, Acta Biomater. 8 (2012) 2331–2339, https://doi.org/10.1016/j.actbio.2012.03.011.

[21] J. Massera, S. Fagerlund, L. Hupa, M. Hupa, Crystallization mechanism of the bioactive glasses 45S5 and S53P4, J. Am. Ceram. Soc. 95 (2012) 607–613, https://doi.org/10.1111/j.1551-2916.2011.05012.x.

[22] H. Fu, M.N. Rahaman, D.E. Day, W. Huang, Long-term conversion of 45S5 bioactive glass-ceramic microspheres in aqueous phosphate solution, J. Mater. Sci. Mater. Med. 23 (2012) 1181–1191, https://doi.org/10.1007/s10856-012-4605-7.

[23] M. Brink, The influence of alkali and alkaline earths on the working range of bioactive glasses, J. Biomed. Mater. Res. 36 (1997) 109–117, https://doi.org/10.1002/(SICI)1097-4636(199707)36:1<109::AID−JBM13>3.0.CO;2-D.

[24] M. Brink, P. Laine, K. Narva, A. Yli-Urpo, Implantation of Bioactive and Inert Glass Fibres in Rats-Soft Tissue Response and Short Term Reactions of the Glass, 10, Elsevier Science, Bioceramics, 1997, pp. 61–64, https://doi.org/10.1016/B978-008042692-1/50015-7.

[25] H. Ylänen, K.H. Karlsson, A. Itälä, H.T. Aro, Effect of SBF on porous bioactive bodies made by sintering bioactive glass microspheres, J. Non Cryst. Solids 275 (2000) 107–115, https://doi.org/10.1016/S0022-3093(00)00245-3.

[26] M. Brink, V. Pitkänen, J. Tikkanen, M. Paajanen, G. Graeffe, Spherical particles of a bioactive glass: Manufacturing and reactions *in vitro*, Bioceramics 9 (1996) 127–130.

[27] A. Itälä, J. Koort, H.O. Ylänen, M. Hupa, H.T. Aro, Biologic significance of surface microroughing in bone incorporation of porous bioactive glass implants, J. Biomed. Mater. Res. A 67 (2003) 496–503, https://doi.org/10.1002/jbm.a.10501.

[28] M.N. Rahaman, D.E. Day, B.S. Bal, Q. Fu, S.B. Jung, L.F. Bonewald, A.P. Tomsia, Bioactive glass in tissue engineering, Acta Biomater. 7 (2011) 2355–2373, https://doi.org/10.1016/j.actbio.2011.03.016.

[29] N. Lindfors, P. Hyvönen, M. Nyyssönen, M. Kirjavainen, J. Kankare, E. Gullichsen, J. Salo, Bioactive glass S53P4 as bone graft substitute in treatment of osteomyelitis, Bone 47 (2010) 212–218, https://doi.org/10.1016/j.bone.2010.05.030.

[30] O. Leppäranta, M. Vaahtio, T. Peltola, D. Zhang, L. Hupa, M. Hupa, H. Ylänen, J. I. Salonen, M.K. Viljainen, E. Eerola, Antibacterial effect of bioactive glasses on clinically important anaerobic bacteria *in vitro*, J. Mater. Sci. 19 (2) (2008) 547–551, https://doi.org/10.1007/s10856-007-3018-5.

[31] E. Munukka, O. Leppäranta, M. Korkeamäki, M. Vaahtio, T. Peltola, D. Zhang, L. Hupa, M. Hupa, H. Ylänen, J.I. Salonen, M.K. Viljainen, E. Eerola, Bactericidal effects of bioactive glasses on clinically important aerobic bacteria, J. Mater. Sci. 19 (1) (2008) 27–32, https://doi.org/10.1007/s10856-007-3143-1.

[32] I. Saarenpää, P. Stoor, J. Frantzén, BAG S53P4 putty as bone graft substitute: a rabbit model, Biomed. Glasses 3 (2017) 30–40, https://doi.org/10.1515/bglass-2017-0003.

[33] P. Sinitsyna, O. Karlström, L. Hupa, *In vitro* dissolution of bioactive glass S53P4 microspheres, J. Am. Ceram. Soc. 105 (2022) 1658–1670, https://doi.org/10.1111/jace.18014.

[34] D. Cacaina, H. Ylänen, S. Simon, M. Hupa, The behaviour of selected yttrium containing bioactive glass microspheres in simulated body environments, J. Mater. Sci. 19 (2008) 1225–1233, https://doi.org/10.1007/s10856-007-3163-x.

[35] V. Pitkänen, J. Tikkanen, M. Paajanen, G. Graeffe, Processing of spherical bioactive glass particles, J. Aerosol Sci. 26 (1995) S831–S832, https://doi.org/10.1016/0021-8502(95)97323-7.

[36] D.E. Day, G.J. Ehrhardt, Glass microspheres, U.S. Patents, 1988.

[37] S.D. Conzone, R.F. Brown, D.E. Day, G.J. Ehrhardt, *In vitro* and *in vivo* dissolution behavior of a dysprosium lithium borate glass designed for the radiation synovectomy treatment of rheumatoid arthritis, J. Biomed. Mater. Res. 60 (2002) 260–268, https://doi.org/10.1002/jbm.10047.

[38] D.E. Day, G.J. Ehrhardt, Composition and method for radiation synovectomy of arthritic joints, U.S. Patents, 1991.

[39] T. Kokubo, H. Takadama, How useful is SBF in predicting *in vivo* bone bioactivity? Biomaterials 27 (2006) 2907–2915, https://doi.org/10.1016/j.biomaterials.2006.01.017.

[40] S. Fagerlund, P. Ek, L. Hupa, M. Hupa, Dissolution kinetics of a bioactive glass by continuous measurement, J. Am. Ceram. Soc. 95 (2012) 3130–3137, https://doi.org/10.1111/j.1551-2916.2012.05374.x.

[41] A.L.B. Maçon, T.B. Kim, E.M. Valliant, K. Goetschius, R.K. Brow, D.E. Day, A. Hoppe, A.R. Boccaccini, Ill Yong Kim, C. Ohtsuki, T. Kokubo, A. Osaka, M. Vallet-Regí, D. Arcos, L. Fraile, A.J. Salinas, A.V. Teixeira, Yu. Vueva, R. M. Almeida, M. Miola, C. Vitale-Brovarone, E. Verné, W. Höland, J.R. Jones, A unified *in vitro* evaluation for apatite-forming ability of bioactive glasses and their variants, J. Mater. Sci. 26 (2015) 1–10, https://doi.org/10.1007/s10856-015-5403-9.

[42] K. Schuhladen, X. Wang, L. Hupa, A.R. Boccaccini, Dissolution of borate and borosilicate bioactive glasses and the influence of ion (Zn, Cu) doping in different solutions, J. Non Cryst. Solids 502 (2018) 22–34, https://doi.org/10.1016/j.jnoncrysol.2018.08.037.

[43] S. Fagerlund, L. Hupa, Melt-derived bioactive silicate glasses, in: Bioactive Glasses Fundamentals, Technology and Applications, 2017, pp. 1–26, https://doi.org/10.1039/9781782622017-00001.

[44] S. Fagerlund, J. Massera, L. Hupa, M. Hupa, T-T-T behaviour of bioactive glasses 1-98 and 13-93, J. Eur. Ceram. Soc. 32 (2012) 2731–2738, https://doi.org/10.1016/j.jeurceramsoc.2011.10.040.

[45] H. Arstila, E. Vedel, L. Hupa, M. Hupa, Predicting physical and chemical properties of bioactive glasses from chemical composition. Part 2: Devitrification characteristics, Glass Technol. 49 (2008) 260–265.

[46] L. Hupa, X. Wang, S. Eqtesadi, Bioactive Glasses, Springer Handbook of Glass, 2019, pp. 813–849, https://doi.org/10.1007/978-3-319-93728-1_23.

[47] G.J. Brentrup, H.M.M. Moawad, L.F. Santos, R.M. Almeida, Structure of Na_2O-CaO-P_2O_5-SiO_2 Glass-Ceramics with multimodal porosity, J. Am. Ceram. Soc. 92 (2009) 249–252, https://doi.org/10.1111/j.1551-2916.2008.02847.x.

[48] D. Bellucci, G. Bolleli, V. Cannillo, A. Cattini, A. Sola, In situ Raman spectroscopy investigation of bioactive glass reactivity: Simulated body fluid solution vs TRIS-buffered solution, Mater. Charact. 62 (2011) 1021–1028, https://doi.org/10.1016/j.matchar.2011.07.008.

[49] G. Miao, Z. Li, Y. Meng, J. Wu, Y. Li, Q. Hu, X. Chen, X. Yang, X. Chen, Preparation, characterization, *in vitro* bioactivity and protein loading/release property of mesoporous bioactive glass microspheres with different compositions, Adv. Powder Technol. 30 (2019) 1848–1857, https://doi.org/10.1016/j.apt.2019.06.002.

[50] L. Hupa, S. Fagerlund, J. Massera, L. Björkvik, Dissolution behaviour of bioactive glasses S53P4 when sodium is replaced by potassium, and calcium with magnesium or strontium, J. Non Cryst. Solids 432 (2016) 41–46, https://doi.org/10.1016/j.jnoncrysol.2015.03.026.

[51] R. Brückner, M. Tylkowski, L. Hupa, D.S. Brauer, Controlling the ion release from mixed alkali bioactive glasses by varying modifier ionic radii and molar ratio, J. Mater. Chem. B 4 (2016) 3121–3134, https://doi.org/10.1039/C5TB02426A.

[52] D. Zhang, M. Hupa, H.T. Aro, L. Hupa, Influence of fluid circulation on in vitro bioactivity of bioactive glass particles, Mater. Chem. Phys. 111 (2008) 497–502, https://doi.org/10.1016/j.matchemphys.2008.04.055.

[53] S. Fagerlund, L. Hupa, M. Hupa, Comparison of reactions of bioactive glasses in different aqueous solutions, Ceram. Trans. 218 (2010) 101–113.

[54] D. Zhang, M. Hupa, L. Hupa, In situ pH within particle beds of bioactive glasses, Acta Biomater. 4 (2008) 1498–1505, https://doi.org/10.1016/j.actbio.2008.04.007.

[55] D.C. Greenspan, J.P. Zhong, G.P. LaTorre, Effect of surface area to volume ratio on in vitro surface reactions of bioactive glass particulates, Bioceramics 7 (1994) 55–60, https://doi.org/10.1016/B978-0-08-042144-5.50012-1.

[56] J.R. Jones, Review of bioactive glass: From hench to hybrids, Acta Biomater. 9 (2013) 4457–4486, https://doi.org/10.1016/j.actbio.2012.08.023.